Few-Layer Graphene Characterization by Near-Field Scanning Microwave Microscopy

Vladimir V. Talanov,[†,⊥,*] Christopher Del Barga,[‡] Lee Wickey,[‡] Irakli Kalichava,[‡] Edward Gonzales,[§] Eric A. Shaner,[§] Aaron V. Gin,[§] and Nikolai G. Kalugin[‡,*]

[†]Semilab USA, LLC, 47 Manning Road, Billerica, Massachusetts 01821, [‡]Materials Engineering Department, New Mexico Tech, Socorro, New Mexico 87801, and [§]Center for Integrated Nanotechnologies and Sandia National Laboratories, Albuquerque, New Mexico 87185. [⊥]Present address: Neocera, LLC, Beltsville, Maryland 20705.

ABSTRACT Near-field scanning microwave microscopy is employed for quantitative imaging at 4 GHz of the local impedance for monolayer and few-layer graphene. The microwave response of graphene is found to be thickness dependent and determined by the local sheet resistance of the graphene flake. Calibration of the measurement system and knowledge of the probe geometry allows evaluation of the AC impedance for monolayer and few-layer graphene, which is found to be predominantly active. The use of localized evanescent electromagnetic field in our experiment provides a promising tool for investigations of plasma waves in graphene with wave numbers determined by the spatial spectrum of the near-field. By using near-field microwave microscopy one can perform simultaneous imaging of location, geometry, thickness, and distribution of electrical properties of graphene without a need for device fabrication.

KEYWORDS: graphene · near-field microwave microscopy · impedance

Single- and few-layer graphene is currently attracting considerable attention because of both the scientific importance (*e.g.*, it is the only material to date with a two-dimensional gas of Dirac fermions) and tremendous potential for various electronic and spintronic applications.[1−3] The relatively high carrier mobility that can be attained in graphene makes it an intriguing material for microwave applications.[4−9] Lin *et al.*[7] demonstrated the first microwave graphene transistor, operating at 4 GHz, and very recently, a transistor with a 100 GHz cutoff frequency.[8] Using a near-field scanning microwave microscope based on atomic-force microscopy (AFM), Kundhikanjana *et al.*[10] obtained the first microwave imaging of graphene flakes, but they do not report any quantitative results of graphene AC impedance.

To further investigate electrodynamic properties of graphene and reveal its potential for microwave applications, we have employed a quantitative approach using a parallel-strip transmission line near-field microwave probe.[11,12] We have found that the microwave impedance of few-layer graphene is thickness dependent and determined by the local sheet impedance of the underlying graphene flake. We demonstrate that near-field microwave microscopy is a feasible alternative to atomic-force microscopy, Raman microscopy,[13−15] low energy electron microscopy (LEEM), or optical methods[16−19] in determination of local graphene thickness.

Near-field microscopy is associated with evanescent waves that occupy a nonradiating, high spatial frequency end of the plane-wave spectrum representation for electromagnetic field. In this regime, $k^2 < k_x^2 + k_y^2 < \infty$, where k is the material complex wavenumber, and k_x and k_y are the in-plane components of the wave vector. Examples of the application of evanescent waves are found in near-field optics and scanning optical microscopy,[20] near-field scanning microwave microscopy,[21−27] negative refraction index materials,[28,29] and the perfect focusing lens.[30] In near-field microwave microscopy, evanescent waves are created by either an electrically small antenna or scattering of the far-field radiation on a subwavelength feature.[31] Since evanescent waves decay exponentially without energy loss, the near-field forms a "cloud" in the vicinity of the probe tip.[32] Assuming that the in-plain spatial frequencies are governed by the probe characteristic size D, such that $|k_x| \approx |k_y| \approx D^{-1}$, and the probe is small enough that $|k|D \ll 1$, the near-field decays into the sample as $\exp(-|k^2 - k_x^2 - k_y^2|^{1/2}z) \approx \exp(-\sqrt{2}z/D)$ yielding $|k_z| \approx \sqrt{2}/D$. Therefore, in all three dimensions the cloud spatial extent is governed by the probe size, which enables a super-resolution imaging. In contrast, the inability of conventional far-field optics to recover evanescent signals causes the spatial

***Address correspondence to:** talanov@neocera.com, nkalugin@nmt.edu.

Received for review March 10, 2010 and accepted May 31, 2010.

Published online June 10, 2010. 10.1021/nn100493f

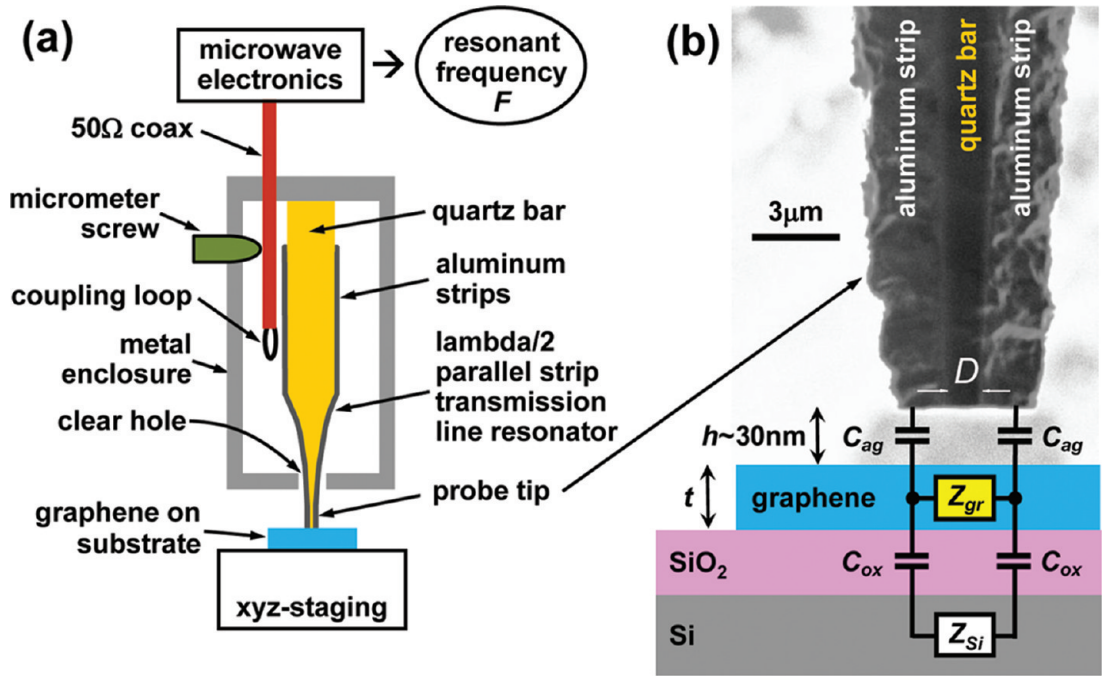

Figure 1. Experimental setup for near-field microwave imaging: (a) diagram of a near-field scanning microwave microscope; (b) scanning electron microscopy (SEM) image of the electrically open tip of the parallel-strip transmission line probe (the spacing between the aluminum strips at the tip is $D \approx 1$ μm), and the equivalent scheme for the tip−sample interaction in the case of graphene on SiO_2/Si substrate. The tip−sample distance h is about 30 nm on graphene; $C_{ag} \approx C_{ox} \approx$ femtoFarad.

frequency of the smallest spot to which the electromagnetic radiation can be converged to be less than $4\pi/\lambda$ (ref 33). Near-field scanning microwave microscopes with the ratio of the probe size to the wavelength down to $10^{-6}-10^{-7}$ have been demonstrated and found to be very useful in nondestructive investigation of local electrodynamic properties of semiconductors, highly correlated electron systems, metamaterials, biological samples, and nanostructures.[12,21−27,31]

Our balanced (differential) near-field probe geometry, having both the signal and ground wires located above the sample (see Figure 1), offers several advantages *versus* the unbalanced STM- and AFM-based near-field microwave probes. First, it allows for truly localized material characterization with the response region defined by the spacing D between the strips, while in an AFM geometry the response may be defined by entire area of graphene flake,[10] which hampers the advantage of AFM's higher physical spatial resolution. Second, an intuitively simple modeling of the probe−sample interaction enables characterization of the absolute local impedance of the sample under study.[34]

The graphene flakes studied in this work were fabricated by a mechanical cleavage method on 300-nm-thick SiO_2 on low resistivity Si wafer. Accurate calibration of the measurement system and knowledge of the tip geometry and tip−sample distance allowed us to evaluate the sheet resistance of exfoliated few-layer graphene at 4 GHz as a function of thickness and/or number of layers. For initial thickness characterization of mechanically cleaved samples, we used "color-code"[1,2] identification of flakes. The final determination of flake thickness was based on AFM data and on the well-known sensitivity of the position and shape of the Raman 2D band around 2700 cm^{-1} to the number of monolayers.[13−15]

Our near-field scanning microwave microscope apparatus is described in detail in the Experimental Methods section (also see ref 12). Briefly, the probe is made of a tapered quartz bar sandwiched between 2-μm-thick aluminum strips (see Figure 1), which forms a balanced parallel-strip transmission line. Such a line carries a TEM wave with highly confined electric field, which uniquely suits the microscope for quantitative measurements.[35] For graphene characterization we fabricated a probe with the quartz cross-section reducing from 1 × 1.2 mm at the probe top down to 1 × 1.2 μm at the electrically open tip end. The probe spatial resolution on the order of one micrometer is governed by the spacing between the aluminum strips at the tip $D \approx$ 1 μm. Microwave imaging was performed in a pixel-by-pixel manner where, at each site, the probe was moved away from a sample and the probe resonant frequency shift $\Delta F = F_0 - F_{sample}$ was recorded, where F_0 is the probe frequency uninfluenced by the sample, and F_{sample} is the frequency measured with the probe in close proximity to the material. Shear-force feedback with optical detection[35] was employed to control the tip−sample distance h with better than 1 nm repeatability.[36] With knowledge of the probe tip geometry

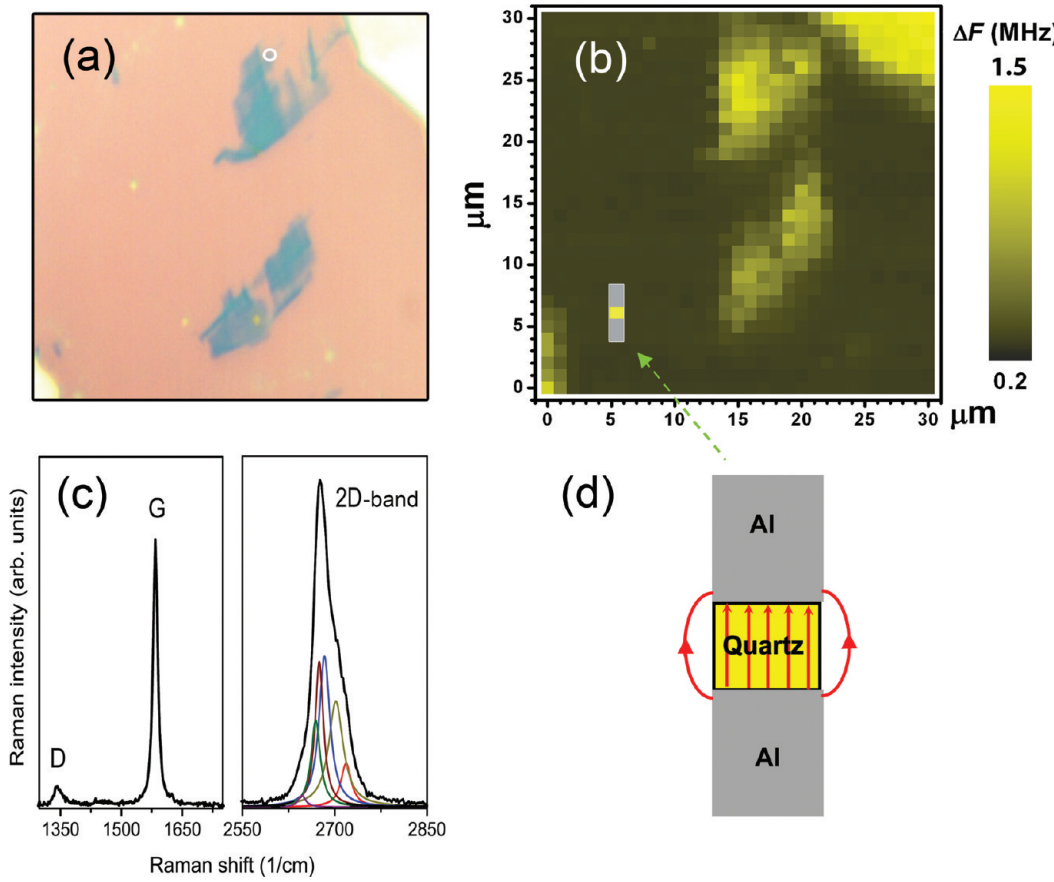

Figure 2. (a) Optical and (b) near-field microwave images of a few-layer graphene flakes with varying number of monolayers. The blue colored fragments in panel a are single- or few-monolayers thick, while the two fragments located in the lower left and upper right corners are 20+ nm thick. The color code in panel b corresponds to the resonant frequency shift of a near-field microwave probe; SiO_2 background yields $\Delta F = 0.33$ MHz. The small cartoon overlaid in the lower left corner of panel b compares the probe tip cross-section to the size of graphene flakes. The tip−sample distance was about 30 nm on graphene. Panel c is the example of 532 nm micro-Raman spectrum taken at the place shown by an encircled area in panel a along with the multiline Lorentzian fitting of 2D band for control of monolayer number at different parts of flakes, which corresponds to 3-layer graphene. (d) Schematic of the in-plane distribution of the sampling microwave current overlaid by the probe tip projection on a sample.

(see Figure 1b) and ΔF measured on a low resistivity silicon wafer, the tip−sample distance on SiO_2/Si was estimated to be about 50 nm (assuming a parallel plate geometry for the air-gap capacitors C_{ag}). All microwave measurements were performed in ambient air without anneal of graphene.

RESULTS AND DISCUSSION

Figure 2a shows an optical image of several exfoliated graphene flakes where color gradation is indicative of flake thickness. The 1 μm spatial resolution microwave image of Figure 2b is formed by the probe resonant frequency shift ΔF acquired as a function of the microscope tip lateral position. As shown, a good correlation exists between the near-field microwave and (far-field) optical image of the few-layer graphene: ΔF is proportional to the thickness-defined color gradation in the optical image. In particular, this is because the size of the near-field probe tip $D \approx 1$ μm is comparable to the optical wavelength.

To confirm the observed phenomena, we measured local thickness at different parts of the various flakes using both AFM and Raman microscopies. A typical example of correlation between the microwave and AFM thickness profile "cuts" is shown in Figures 3a,b for a graphene flake shown in Figures 3c,d using microwave and AFM imaging, respectively. The white arrows in Figures 3c,d show the location and direction of the "cut" shown in Figures 3a,b. From the microwave and AFM cross sections it is clear that the thicker parts of the flake produce larger frequency shifts. From the microwave, AFM, and Raman data we were able to extract ΔF *versus* graphene thickness as shown by symbols in Figure 4. To explain the observed dependence, we developed the following two-dimensional (2D) and three-dimensional (3D) models for graphene flakes thinner and thicker than about 10 nm, respectively.

To derive an impedance for few-layer graphene, we recall that in the absence of interlayer interaction the screening due to a "sandwich" of two-dimensional conducting layers can be represented as a sum of the

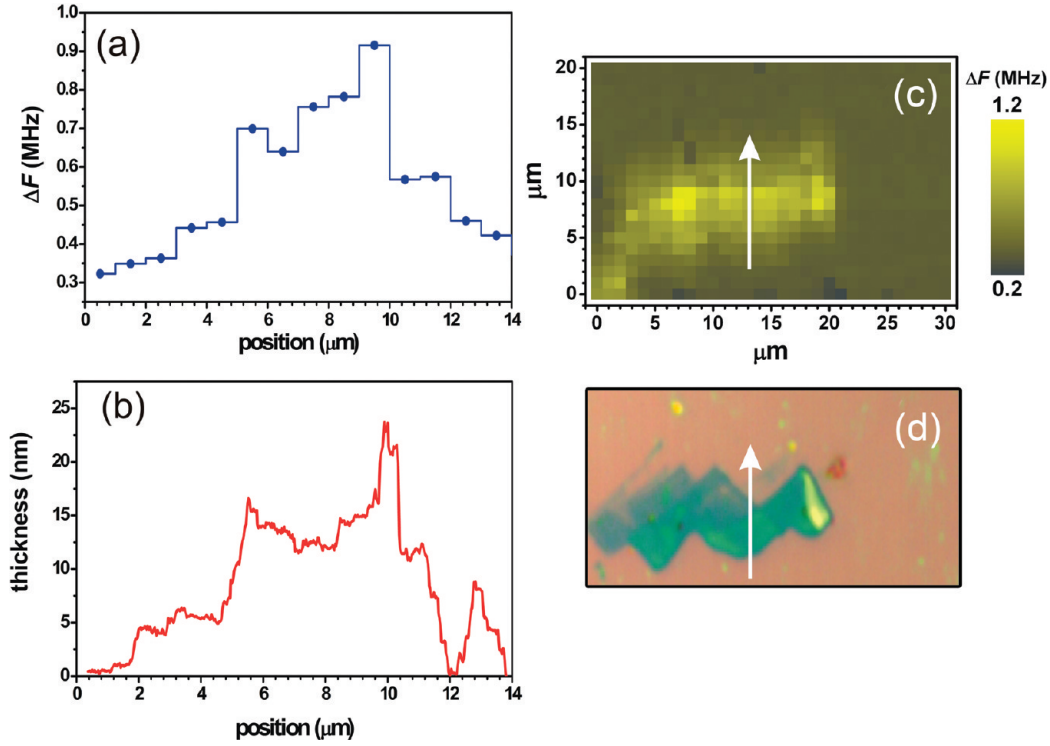

Figure 3. Example of the microwave frequency shift (a) and corresponding AFM-measured thickness profile (b) for a few-layer graphene flake shown in panels c and d. Panels c and d are the near-field microwave and the optical images and the optical of graphene flake, respectively. White arrows in panels c and d show the location and direction of the microwave and AFM profile "cuts" in panels a and b.

screening due to individual layers.[37,38] Following the results of ref 39 and ref 40, the impedance presented to our near-field probe by a two-dimensional system is

$$Z_{gr2D} = \frac{g + 2a}{N}\frac{1 + i\omega\tau}{\sigma_{2D}} \qquad (1)$$

where $g \approx 0.36$ is the form-factor accounting for the microwave current distribution in the graphene outside

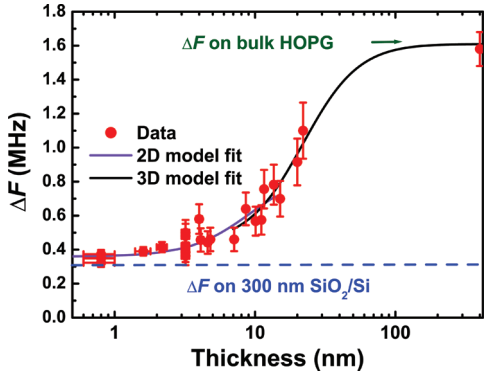

Figure 4. Probe frequency shift Δ*F vs* AFM-defined graphene thickness on a semilog scale. The blue dashed line represents Δ*F* observed on bare 300-nm-thick SiO_2/Si. The vertical error bars in our diagram are due to the difference in spatial resolution between the microwave and AFM images. The uncertainty of the AFM thickness measurement (reflected in horizontal error bars) is about ±0.2 nm. For mono-, bi-, and trilayer graphene, using both AFM and Raman thickness determination, we minimized the vertical error. Solid lines are the fits to 2D and 3D models (see text).

of the two areas projected by the aluminum strips[31,41] (see Figure 2d), $a \approx (2\ \mu m/1.2\ \mu m)/3 = 1.1$ is the form-factor[42] describing the contribution from the graphene region projected by the aluminum strip (see Figure 1b), $N = t/t_1$ is the number of layers in the graphene stack; t is the stack thickness, t_1 is the monolayer thickness, and τ is the scattering time. In eq 1 $\sigma_{2D} = \mu n_{2D} e$ is the semiclassical two-dimensional low-frequency Drude conductivity, with μ being the carrier mobility, n_{2D} the carrier density per unit area, and e the electron charge. The use of the Drude model is justified for the Fermi gas of electrons. However, the transition from Dirac to Fermi gas of electrons in monolayer and bilayer graphene takes place at elevated temperatures and/or high electron concentrations (see refs 43−45). In our nonannealed dirty samples, we expect rather high carrier concentrations, thus making the above "high-carrier-density" conductivity applicable. Let us point out that relation (1) is valid in the long-wavelength limit $q \ll k_F$, where q is the plasmon wavenumber and k_F is the Fermi momentum. The wavenumber (or the effective sample size) in our experiment is defined by the spacing between the aluminum strips at the tip, that is, $q \approx D^{-1} \approx 1\ \mu m^{-1}$. Using $n_{2D} \approx 10^{11}-10^{12}\ cm^{-2}$, we estimate for graphene $k_F = (4\pi n_{2D}/g_s g_v)^{1/2} \approx 100\ \mu m^{-1}$, with $g_s = 2$ and $g_v = 2$ being the spin and valley degeneracy, respectively.[46] Therefore, the long-wavelength limit is valid in our case.

Similarly to eq 1, the impedance presented to the probe by thicker graphene (or graphite) can be found as follows:

$$Z_{gr3D} = \frac{g + 2a}{t}\frac{1 + i\omega\tau}{\sigma_{3D}} \quad (2)$$

where $\sigma_{3D} = \mu n_{3D} e$ is the three-dimensional low-frequency Drude conductivity with n_{3D} being the carrier density per unit volume, and t being the graphite thickness.

From the lumped element scheme in Figure 1b, neglecting Z_{Si} in comparison to $1/\omega C_{ox}$, the total tip susceptance terminating the parallel strip resonator can be calculated as follows:

$$B_t = \frac{\omega C_{ag}(4G_{gr}^2 + (2B_{gr} + \omega C_{ox})(2B_{gr} + \omega(C_{ag} + C_{ox})))}{8G_{gr}^2 + 2(2B_{gr} + \omega(C_{ag} + C_{ox}))^2} \quad (3)$$

where $G_{gr} = Re[1/Z_{gr}]$ and $B_{gr} = Im[1/Z_{gr}]$ are the graphene conductance and susceptance found from eq 1 and eq 2 for 2D and 3D cases, respectively. Finally, using eq E3a from the Experimental Methods section of our article, the probe frequency shift is calculated as follows:

$$\Delta F = F_0 - F_{sample} = \pi^{-1} F_0 Z_0 B_t \quad (4)$$

where F_0 is the probe frequency with the tip retracted from the sample, F_{sample} is the probe frequency in the shear-force, $Z_0 \approx 100\ \Omega$ is the characteristic impedance of the parallel strip transmission line, and B_t is the tip susceptance in the shear-force given by eq 3. In eq 4 the susceptance of the tip retracted from the sample is ignored in comparison to B_t because the terminating capacitance of the fully retracted tip of about $\varepsilon_0 D \approx 10^{-17} F$ (ε_0 is the vacuum permittivity) is much less than the air-gap capacitance $C_{ag} \approx 10^{-15} F$. To extract the graphene characteristics from our data, according to eq 3, we also need to know C_{ag} and the silicon dioxide capacitance C_{ox}. C_{ag} is determined experimentally by measuring $\Delta F = F_0^2 Z_0 C_{ag}$ on implanted Si wafer with 100 Ω sheet resistance. After that, C_{ox} is determined from the measurement on SiO_2 film (outside of graphene flakes) where $\Delta F = F_0^2 Z_0 C_{ag} C_{ox}/(C_{ag} + C_{ox}) = 0.33$ MHz.

The results of analyzing our experimental data using the above models are shown in Figure 4 by solid lines. For graphene flakes thinner than 10 nm we fit ΔF given by eq 4 with the aid of eq 1 and eq 3, using σ_{2D} and τ as the free-fitting parameters. We obtain $\sigma_{2D} = 1.4 \times 10^{-6}$ S and $\tau < 10^{-12}$ s. The latter confirms that at 4 GHz we operate in a diffusive transport regime with $\omega\tau \ll 1$, where the impedance is mostly active and defined by the DC conductivity. This agrees with results of ref 47, where depending on the carrier concentration, the scattering time in graphene was found to range from 10^{-14} to 10^{-12} s.

For thicker graphite with $t > 10$ nm, using σ_{3D} and τ as the free-fitting parameters, we fit eq 4 with the aid of eq 2 and eq 3. The obtained values are $\sigma_{3D} = 1.1$ kS/m and $\tau = 3 \times 10^{-12}$ s. Such a short scattering time shows that, again, our samples exhibit diffusive transport.

Our two-dimensional model does not take into account all specifics of the Dirac band structure of graphene.[38,44−46,48] At the same time, it adequately describes the overall behavior of the probe frequency shift due to multilayer graphene/graphite over a wide range of thicknesses. Application of this model for few-layer graphene allowed us to directly restore the sheet resistance for mono-, bi-, and trilayer graphene from the experimental data. For monolayer, bilayer, and trilayer graphene, we obtained a 4 GHz sheet resistance of ~700 kΩ/□, ~350 kΩ/□, and ~240 kΩ/□, respectively. The determined value of sheet resistance for our monolayer graphene is significantly higher than ~2.1 kΩ/□ reported in ref 4 for pristine material. However, our value is consistent with the hundreds of kΩ values of DC resistance found in contaminated non-annealed monolayer graphene.[10] Since in our experiment we have also used nonannealed samples in ambient air, the observed values of impedance are reasonable.

Further analysis of our experimental data requires significant development of theories describing interaction between our balanced probe geometry and a two-dimensional gas for both "classical"[49−51] and Dirac electrons.[38,44,45,48] The use of a localized evanescent electromagnetic field in our experiment provides for unusually large plasmon wave numbers in graphene $q \approx D^{-1} \geq 10^4$ cm^{-1}. For correct description of conductivity in this case, the screening properties (plasma effects) of the two-dimensional electron system will become important and need to be included in a full analysis. We anticipate that future efforts involving dynamic control of the carrier density of graphene samples under test will be performed in order to develop a better understanding of probe/sample interaction as well as high frequency graphene conductivity.

The use of a parallel-strip transmission line probe in near-field microwave microscopy opens up other new possibilities in graphene research. One interesting question is the influence of stacking of graphene sheets on electrical properties of a few-layer graphene. Significant modifications of the energy band spectra of few-layer graphene near the charge neutrality point due to different stacking of adjacent monolayers[52] lead to observable differences in Raman[53] and infrared spectra.[54] Theory[38] also predicts the decrease of electromagnetic field screening in the case of non-Bernal stacking. One of the next steps investigating graphene with our technique will be to work with larger annealed graphene flakes to allow investigations of the influence of stacking on electrodynamic response and screening properties of graphene stack that are not masked by doping or

limited by spatial resolution. Investigation of high quality gated Hall-bar samples comprising one or few-layer graphene material is also of significant interest in order to study the microwave impedance under various charge configurations. Here, by gaining control over the carrier density in the graphene layers, we should be able to further investigate the two-dimensional properties of the material and refine the electrodynamic analysis presented in this work. Our probe geometry should also allow for direct investigation of ballistic transport in materials with the coherence length greater than 1 μm, such as graphene or more conventional two-dimensional electron gas systems.

SUMMARY AND CONCLUSION

We performed near-field microwave imaging and electrical characterization of few-layer graphene flakes. Near-field microwave microscopy is shown to be a viable method for the electronic transport characterization in graphene, which can be used as an alternative method for thickness determination of graphene. The observed resonant frequency-shift sensitivity to local thickness of graphene may be explained by the similarity of graphene behavior at 4 GHz to that of a thin conductive film. By using an electrodynamic model relating the frequency shift to the tip impedance, we evaluated the sheet impedance for thicknesses ranging from single and few layer graphene to bulk graphite. Our approach may be useful for the design of future graphene-based microwave devices, quality control in large area graphene sheets, or investigations of how chemical or electrical doping of graphene influences the microwave material properties.

EXPERIMENTAL METHODS

For fabrication of graphene flakes we used a mechanical cleavage of highly ordered pyrolytic graphite (HOPG) SPI-I from Structure Probe Inc. on 300-nm-thick ICPCVD-grown SiO_2 on low resistivity Si wafer. For thickness characterization of mechanically cleaved samples, we used "color-code"[1,2] identification of flakes in Nikon Eclipse 150 optical microscope. The final determination of flake thickness was based on AFM data and on the well-known sensitivity of the position of the Raman 2D band around 2700 cm^{-1} to the number of monolayers.[13−15] Atomic force microscopy is a standard technique for graphene thickness determination. In our measurements, we achieved about ±0.2 nm uncertainty in thickness determination by AFM which allowed us to distinguish between the single and few-layer graphene sheets. For Raman measurements of graphene thickness we used a well-known dependence of 2D-Raman-band on the number of monolayers for structurally uniform graphene.[22−24] We analyzed the shape of 2D-band by comparing experimental Raman spectra with the results of numerical multi-Lorentzian fitting. The number of Lorentzian peaks forming the shape of 2D-band, its positions and widths clearly indicate the number of monolayers.[13−15] The Raman studies were performed using a HORIBA Jobin-Yvon LabRAM Aramis micro-Raman system. The 532 nm line of a solid state laser was used for excitation. Structural information on the graphene flakes was obtained using atomic force microscopy (AFM) using a Digital Instruments Dimension 3100 scanning probe microscope.

Our near-field scanning microwave microscope utilizes a probe based on a balanced parallel-strip transmission line resonator.[12] It is made of a tapered quartz bar sandwiched between 2-μm-thick aluminum strips (see Figure 1) with the quartz cross-section reducing from 1 × 1.2 mm at the probe top down to 1 × 1.2 μm at the tip end (see Figure 1b). The probe was microfabricated as follows. First, a quartz micropipette is pulled with a commercial UV laser micropipette puller from Sutter Instrument, Inc. This is followed by depositing 2-μm-thick aluminum onto two wide sides of the micropipette. Then, the unwanted aluminum deposits are removed selectively from the narrow sides by exposing the entire probe to a large diameter ion beam normally incident to the narrow sides. Finally, the electrically open tip end facet is micromachined by a focused ion beam[55] where a separation between two aluminum strips is about 1 μm (see Figure 1b), which eventually governs the microscope spatial resolution (see Figure 2d). The obtained transmission line is capable of carrying a TEM wave with electric field mostly confined between the two aluminum strips (similar to that of a parallel plate capacitor).[56] The balanced probe design virtually eliminates both the stray field and far-field radiation so the microscope response is entirely defined by a sample area projected by the probe tip, unlike in unbalanced STM[21] or AFM-based[10,22] near-field probe geometries where return path for the sampling current is typically indeterminate.

To achieve the desirable microscope sensitivity, the probe tip impedance of the order of 10^5-10^6 Ω is matched to the 50 Ω coaxial feedline impedance by forming a 24-mm-long half-lambda transmission line resonator with resonant frequency of 4.2 GHz and unloaded Q-factor greater than 100. A magnetic loop, adjusted by a fine micrometer screw, provides a critical coupling to the resonator with a return loss greater than 60 dB. The resonator and coupling loop are mounted inside a metallic enclosure with the resonator tapered end portion protruding a few millimeters out through a clear hole in the enclosure end wall. The typical magnitude of microwave electric field at the end of the tip exposed to the sample was on the order of 1−2 kV/cm.

Since the probe tip is much smaller than the microwave radiation wavelength, a lumped element approach is adequate for describing the probe−sample interaction. To find a relationship between the probe tip admittance $Y = G + iB$ (G and B are the tip conductance and susceptance, respectively) and the resonant frequency F, consider a half-wavelength resonator formed by a parallel strip transmission line terminated with an electric near-field probe on one end. The resonant condition is:[57]

$$\exp(-i2\gamma L)\Gamma_t\Gamma_0 = \exp(-i2\pi n) \quad \text{(E1)}$$

where $\gamma = \gamma_1 - i\gamma_2$ is the complex propagation constant, L is the resonator length, Γ_t is the probe tip reflection coefficient $\Gamma_t \approx 1 - 2Z_0Y_t$, Z_0 is the characteristic impedance of the parallel strip transmission line, Γ_0 is the reflection coefficient from the resonator opposite end, and $n = 1, 2, \ldots$ is the mode number. Substituting the complex angular frequency $\tilde{\omega} = \omega_1 + i\omega_2$ and $\Gamma_0 = 1$ into (E1), expanding $\exp(-i2\gamma L)$ around $\gamma L = \pi n$, and neglecting the higher-order terms due to $\gamma_2 \ll \gamma_1$, $\omega_2 \ll \omega_1$ and $Z_0|Y_t| \ll 1$ we obtain for the relative change in $\tilde{\omega}$:

$$\frac{\Delta\tilde{\omega}}{\tilde{\omega}} = -i\frac{Z_0}{\pi}\Delta Y_t \quad \text{(E2)}$$

Separating the real and imaginary parts in eq E2 yields for the small changes in $F = \omega_1/2\pi$ and $Q^{-1} = 2\omega_2/\omega_1$:

$$\frac{\Delta F}{F} = -\frac{Z_0}{\pi}\Delta B_t \quad \text{(E3a)}$$

$$\Delta\left(\frac{1}{Q}\right) = \frac{2Z_0}{\pi}\Delta G_t \qquad \text{(E3b)}$$

While the *Q*-factor measurements were not available at the time of our experiment, we present the last equation here for the sake of completeness. Expression E3a recaptures the result of ref 58 for the case of a low-loss sample.

Shear-force feedback[36,59] with optical detection[35] is employed in our microscope to control the probe-sample distance h with better than 1 nm repeatability. The tapered quartz bar forms a cantilevered beam in which a fundamental mode at 2.6 kHz is excited by dithering the probe enclosure with nanometer amplitude using a piezo tube. The probe tip is illuminated with a laser beam projecting onto a photodetector, which AC output depends on the tip vibration amplitude that is a strong function of the tip−sample distance for $h < 100$ nm. After passing through a lock-in amplifier the signal is fed into a closed-loop controller, moving up and down a precision piezo *z*-stage carrying the probe enclosure. To eliminate the thermal drift in the tip−sample air-gap the closed-loop set point is recalculated every time the probe pulled away from a sample.

The shear-force tip−sample distance in our microscope is typically independent of the sample material.[35] From measuring ΔF on a low resistivity silicon wafer and knowing the probe tip geometry (see Figure 1b) the tip−sample distance is estimated to be about 50 nm (a parallel-plate geometry is assumed for the air-gap capacitors in Figure 1b). However, in the case of graphene as well as HOPG (the same sample was used for fabricating the graphene flakes), we noticed a reduction in the tip−sample distance by about 30−40% in comparison to that on Si or SiO_2/Si samples. By recording a probe response at the very beginning of the tip coming into a shear-force with the sample, we were able to mitigate the problem of occasional flake damage and collect reliable data. While the nature of the shear-force interaction in scanning probe microscopy is not well understood yet,[36] the observed issue can be attributed to the fact that graphite is a strongly hydrophobic material.

All microwave measurements were performed in ambient air without a preliminary anneal of graphene. The imaging was performed in a pixel-by-pixel manner where, at each site, after measuring a sample the probe was pulled about 30 μm away from a sample and the resonant frequency shift $\Delta F = F_0 - F_{sample}$ was recorded, where F_0 is the probe frequency uninfluenced by the sample. Using this procedure, the terminating capacitance of the tip fully retracted is on the order of $\varepsilon_0 D \approx 10aF$. This value is negligible compared to all other impedance values encountered and serves as a reasonable reference point. The microwave electronics based on a closed-loop frequency tracking circuit[12] allows monitoring the probe resonant frequency with better than 1 kHz precision. This is enough to distinguish between one, two, and more graphene layers in our experiment (the observed in our experiment frequency shift difference between one- and two-monolayers-thick graphene was about 30−40 kHz, what is about 10 times the precision of the frequency shift determination).

Acknowledgment. This work was performed, in part, at the Center for Integrated Nanotechnologies, a U.S. Department of Energy, Office of Basic Energy Sciences user facility at Sandia National Laboratories (Contract DE-AC04-94AL85000). We gratefully acknowledge support from the NASA NM Space Grant Consortium program and from the LANL-NMT MOU program supported by UCDRD. We are thankful to Dr. Dmitry Smirnov for fruitful discussions and to Mr. Chad Cooper and Mr. B. Bobrzynski for experimental assistance.

REFERENCES AND NOTES

1. Geim, A. K.; Novoselov, K. S. The Rise of Graphene. *Nat. Mater.* **2007**, *6*, 183–191.
2. Novoselov, K. S.; Geim, A. K.; Morozov, S. V.; Jiang, D.; Zhang, Y.; Dubonos, S. V.; Grigorieva, I. V.; Firsov, A. A. Electric Field Effect in Atomically Thin Carbon Films. *Science* **2004**, *306*, 666–669.
3. Tan, Y. W.; Zhang, Y.; Bolotin, K.; Zhao, Y.; Adam, S.; Hwang, E. H.; Das Sarma, S.; Stormer, H. L.; Kim, P. Measurement of Scattering Rate and Minimum Conductivity in Graphene. *Phys. Rev. Lett.* **2007**, *99*, 246803. -1−4.
4. Jeon, D.-Y.; Lee, K. J.; Kim, M.; Kim, D. C.; Chung, H.-J.; Woo, Y.-S.; Seo, S. Radio-Frequency Electrical Characteristics of Single Layer Graphene. *Jpn. J. Appl. Phys.* **2009**, *4*, 091601–091603.
5. Neugebauer, P.; Orita, M.; Faugeras, C.; Barra, A.-L.; Potemski, M. How Perfect Graphene Can Be. *Phys. Rev. Lett.* **2009**, *103*, 136403. -1−4.
6. Deligeorgis, G.; Dragoman, M.; Neculoiu, D.; Dragoman, D.; Konstantinidis, G.; Cismaru, A.; Plana, R. Microwave Propagation in Graphene. *Appl. Phys. Lett.* **2009**, *95*, 073107. -1−3.
7. Lin, Y.-M.; Jenkins, K. A.; Valdes-Garcia, A.; Small, J. P.; Farmer, D. B.; Avouris, P. Operation of Graphene Transistors at Gigahertz Frequencies. *Nano Lett.* **2009**, *9*, 422–426.
8. Lin, Y.-M.; Dimitrakopoulos, C.; Jenkins, K. A.; Farmer, D. B.; Chiu, H.-Y.; Grill, A.; Avouris, P. 100-GHz Transistors from Wafer-Scale Epitaxial Graphene. *Science* **2010**, *327*, 662.
9. Krupka, J.; Stupinski, W. Measurements of the Sheet Resistance and Conductivity of Thin Epitaxial Graphene and SiC Films. *Appl. Phys. Lett.* **2010**, *96*, 082101. 1−3.
10. Kundhikanjana, W.; Lai, K.; Wang, H.; Dai, H.; Kelly, M. A.; Shen, Z.-X. Hierarchy of Electronic Properties of Chemically Derived and Pristine Graphene Probed by Microwave Imaging. *Nano Lett.* **2009**, *9*, 3762–3765.
11. Klein, N.; Lahl, P.; Poppe, U.; Kadlec, F.; Kuzel, P. A Metal-Dielectric Antenna for Terahertz Near-Field Imaging. *J. Appl. Phys.* **2005**, *98*, 014910. -1−5.
12. Talanov, V. V.; Scherz, A.; Moreland, R. L.; Schwartz, A. R. A Near-Field Scanned Microwave Probe for Spatially Localized Electrical Metrology. *Appl. Phys. Lett.* **2006**, *88*, 134106. 1−3.
13. Ferrari, A. C.; Meyer, J. C.; Sardaci, V.; Casiragi, C.; Lazzeri, M.; Mauri, F.; Piscanec, S.; Jiang, D.; Novoselov, K. S.; Roth, S.; Geim, A. K. Raman Spectrum of Graphene and Graphene Layers. *Phys. Rev. Lett.* **2006**, *97*, 187401. -1−4.
14. Graf, D.; Molitor, F.; Ensslin, K.; Stampfer, C.; Jungen, A.; Hierold, C.; Wirtz, L. Spatially Resolved Raman Spectroscopy of Single- and Few-Layer Graphene. *Nano Lett.* **2007**, *7*, 238–242.
15. Malard, L. M.; Mafra, D. L.; Doorn, S. K.; Pimenta, M. A. Resonance Raman Scattering in Graphene: Probing Phonons and Electrons. *Solid State Commun.* **2009**, *149*, 1136–1139.
16. Hibino, H.; Kageshima, H.; Maeda, F.; Nagase, M.; Kobayashi, Y.; Yamaguchi, H. Microscopic Thickness Determination of Thin Graphite Films Formed on SiC from Quantized Oscillation in Reflectivity of Low-Energy Electrons. *Phys. Rev.* **2008**, *B 77*, 075413. -1−7.
17. Fei, Z.; Shi, Y.; Pu, L.; Gao, F.; Liu, Y.; Sheng, L.; Wang, B.; Zhang, R.; Zheng, Y. High-Energy Optical Conductivity of Graphene Determined by Reflection Contrast Spectroscopy. *Phys. Rev.* **2008**, *B 78*, 201402 (R). -1−4.
18. Ni, Z. H.; Wang, H. M.; Kasim, J.; Fan, H. M.; Yu, T.; Wu, Y. H.; Feng, Y. P.; Shen, Z. X. Graphene Thickness Determination Using Reflection and Contrast Spectroscopy. *Nano Lett.* **2007**, *7*, 2758–2763.
19. Mak, K. F.; Lui, C. H.; Shan, J.; Heinz, T. F. Observation of an Electric-Field-Induced Band Gap in Bilayer Graphene by Infrared Spectroscopy. *Phys. Rev. Lett.* **2009**, *102*, 256405. -1−4.
20. Novotny, L.; Hecht, B. *Principles of Nano-optics*; Cambridge University Press: Cambridge, UK, 2006.
21. Stranick, S. J.; Weiss, P. S. A Versatile Microwave Frequency-Compatible Scanning Tunneling Microscope. *Rev. Sci. Instrum.* **1993**, *64*, 1232–1234.
22. Cho, Y.; Kirihara, A.; Saeki, T. Scanning Nonlinear Dielectric Microscope. *Rev. Sci. Instrum.* **1996**, *67*, 2297–2303.
23. Golosovsky, M.; Davidov, D. Novel Millimeter-Wave Near-Field Resistivity Microscope. *Appl. Phys. Lett.* **1996**, *68*, 1579–1581.

24. Lu, Y.; Wei, T.; Duewer, F.; Lu, Y.; Ming, N.; Schultz, P. G.; Xiang, X.-D. Nondestructive Imaging of Dielectric-Constant Profiles and Ferroelectric Domains with a Scanning-Tip Microwave Near-Field Microscope. *Science* **1997**, *276*, 2004–2006.
25. Van der Weide, D. W. Localized Picosecond Resolution with a Near-Field Microwave/Scanning-Force Microscope. *Appl. Phys. Lett.* **1997**, *70*, 677–679.
26. Steinhauer, D. E.; Vlahacos, C. P.; Dutta, S.; Wellstood, F. C.; Anlage, S. M. Surface Resistance Imaging with a Scanning Near-Field Microwave Microscope. *Appl. Phys. Lett.* **1997**, *71*, 1736–1738.
27. Tabib-Azar, M.; Su, D.-P.; Pohar, A.; LeClair, S. R.; Ponchak, G. 0.4 μm Spatial Resolution with 1 GHz (λ = 30 cm) Evanescent Microwave Probe. *Rev. Sci. Instrum.* **1999**, *70*, 1725–1729.
28. Pendry, J. B. Negative Refraction Makes a Perfect Lens. *Phys. Rev. Lett.* **2000**, *85*, 3966–3969.
29. Pendry, J. B. Pendry Replies. *Phys. Rev. Lett.* **2001**, *87*, 249704–1.
30. Merlin, R. Radiationless Electromagnetic Interference: Evanescent-Field Lenses and Perfect Focusing. *Science* **2007**, *317*, 927–929.
31. Anlage, S. M.; Talanov, V. V.; Schwartz, A. R. in *Scanning Probe Microscopy: Electrical and Electromechanical Phenomena at the Nanoscale*; Kalinin, S., Gruverman, A., Eds.; Springer Science: New York, 2007; pp 215−253.
32. Ohtsu, M.; Kobayashi, K. *Optical Near Fields: Introduction to Classical and Quantum Theories of Electromagnetic Phenomena at the Nanoscale*; Springer Science: New York, 2004.
33. Abbe, E. Beitraumlige zur Theorie des Mikroskops und der Mikroskopischen Wahrnehmung. *Archiv Mikroskop. Anat. Entwicklungsmech.* **1873**, *9*, 413–468.
34. Talanov, V. V.; Scherz, A.; Schwartz, A. R. Noncontact Electrical Metrology of Cu/low-*k* Interconnect for Semiconductor Production Wafers. *Appl. Phys. Lett.* **2006**, *88*, 262901. -1−3.
35. Talanov, V. V.; Scherz, A.; Moreland, R. L.; Schwartz, A. R. Noncontact Dielectric Constant Metrology of Low-*k* Interconnect Films Using a Near-Field Scanned Microwave Probe. *Appl. Phys. Lett.* **2006**, *88*, 192906. -1−3.
36. Lapshin, D. A.; Letokhov, V. S.; Shubeita, G. T.; Sekatskii, S. K.; Dietler, G. Shear Force Distance Control in a Scanning Near-Field Optical Microscope: In Resonance Excitation of the Fiber Probe *versus* Out of Resonance Excitation. *Ultramicroscopy* **2004**, *99*, 227–233.
37. Visscher, P. B.; Falikov, L. M. Dielectric Screening in a Layered Electron Gas. *Phys. Rev. B* **1971**, *3*, 2541–2547.
38. Guinea, F. Charge Distribution and Screening in Layered Graphene Systems. *Phys. Rev. B* **2007**, *75*, 235433. 1−7.
39. Ryzhii, V.; Satou, A.; Shur, M. S. Admittance of a Slot Diode with a Two-Dimensional Electron Channel. *J. Appl. Phys.* **2003**, *93*, 10041–10045.
40. Kang, S.; Burke, P. J.; Pfeiffer, L. N.; West, K. W. AC Ballistic Transport in a Two-Dimensional Electron Gas Measured in GaAs/AlGaAs Heterostructures. *Phys. Rev. B* **2005**, *72*, 165312. -1−5.
41. For a near-field probe formed by the open ended transmission line $g = Z_{0vac}/120\pi$, where Z_{0vac} is the line characteristic impedance for the vacuum dielectric filling. To calculate Z_{0vac} of parallel strip transmission line we used, for example, Bahl, I. J.; Gang, R. Simple and Accurate Formulas for a Microstrip with Finite Strip Thickness. *Proc. IEEE* **1977**, *65*, 1611–1612.
42. Burke, P. J.; Spielman, I. B.; Eisenstein, J. P.; Pfeiffer, L. N.; West, K. W. High Frequency Conductivity of the High-Mobility Two-Dimensional Electron Gas. *Appl. Phys. Lett.* **2000**, *76*, 745–747.
43. Adam, S.; Hwang, E. H.; Galitski, V. M.; Das Sarma, S. A Self-Consistent Theory for Graphene Transport. *Proc. Natl. Acad. Sci. U.S.A.* **2007**, *104*, 18392–18397.
44. Wang, X.-F.; Chakraborty, T. Coulomb Screening and Collective Excitations in a Graphene Bilayer. *Phys. Rev. B* **2007**, *75*, 041404(R). -1−4.
45. Wang, X.-F.; Chakraborty, T. Coulomb Screening and Collective Excitations in Biased Bilayer Graphene. *Phys. Rev. B* **2010**, *81*, 081402(R). -1−4.
46. Hwang, E. H.; Das Sarma, S. Dielectric Function, Screening, and Plasmons in Two-Dimensional Graphene. *Phys. Rev.B.* **2007**, *75*, 205418. -1−6.
47. Tan, Y.-W.; Zhang, Y.; Bolotin, K.; Zhao, Y.; Adam, S.; Hwang, E. H.; Das Sarma, S.; Stormer, H. L.; Kim, P. Measurement of Scattering Rate and Minimum Conductivity in Graphene. *Phys. Rev. Lett.* **2007**, *99*, 246803. -1−4.
48. Ryzhii, V.; Satou, A.; Otsuji, T. Plasma Waves in Two-Dimensional Electron-Hole System in Gated Graphene Heterostructures. *J. Appl. Phys.* **2007**, *101*, 024509. -1−5.
49. Stern, F. Polarizability of a Two-Dimensional Electron Gas. *Phys. Rev. Lett.* **1967**, *188*, 546–548.
50. Allen, S. J.; Tsui, D. C.; Logan, R. A. Observation of the Two-Dimensional Plasmon in Silicon Inversion Layers. *Phys. Rev. Lett.* **1977**, *38*, 980–983.
51. Shaner, E. A.; Lyon, S. A. Time-Resolved Impulse Response of the Magnetoplasmon Resonance in a Two-Dimensional Electron Gas. *Phys. Rev. B* **2002**, *66*, 041402(R). -1−3.
52. Castro Neto, A. H.; Peres, N. M. R.; Novoselov, K. S.; Geim, A. K. The Electronic Properties of Graphene. *Rev. Mod. Phys.* **2009**, *81*, 109–162.
53. Poncharal, P.; Ayari, A.; Michel, T.; Sauvajol, J.-L. Effect of Rotational Stacking Faults on the Raman Spectra of Folded Graphene. *Phys. Rev.* **2009**, *B 79*, 195417. -1−4.
54. Mak, K. F.; Shan, J.; Heinz, T. F. Electronic Structure of Few-Layer Graphene: Experimental Demonstration of Strong Dependence on Stacking Sequence. *Mater. Sci., Condens. Matter*, published online February 10, 2010, http://arxiv.org/abs/1002.2225.
55. Pilevar, S.; Edinger, K.; Atia, W.; Smolyaninov, I.; Davis, C. Focused Ion-beam Fabrication of Fiber Probes with Well-Defined Apertures for Use in Near-Field Scanning Optical Microscopy. *Appl. Phys. Lett.* **1998**, *72*, 3133–3135.
56. Talanov, V. V.; Scherz, A.; Schwartz, A. R. A Microfabricated Near-Field Scanned Microwave Probe for Noncontact Dielectric Constant Metrology of Low-*k* Films. *IEEE MTT-S Int. Microwave Symp. Dig.* **2006**, 1618–1621.
57. Weinstein, L. A. *Theory of Diffraction and Method of Factorization*; Sovetskoe Radio, Moscow, 1966.
58. Reznik, A. N.; Yurasova, N. V. Electrodynamics of Microwave Near-Field Probing: Application to Medical Diagnostics. *J. Appl. Phys.* **2005**, *98*, 114701. -1−9.
59. Betzig, E.; Finn, P. L.; Weiner, J. S. Combined Shear Force and Near-Field Scanning Optical Microscopy. *Appl. Phys. Lett.* **1992**, *60*, 2484–2486.